Matter and Radiation at Extremes

RESEARCH ARTICLE

scitation.org/journal/mre

Density-dependent shock Hugoniot of polycrystalline diamond at pressures relevant to ICF

Cite as: Matter Radiat. Extremes 6, 035902 (2021); doi: 10.1063/5.0039062
Submitted: 30 November 2020 • Accepted: 14 February 2021 •
Published Online: 30 March 2021

View Online Export Citation CrossMark

Peng Wang,[1,2] Chen Zhang,[1] Shaoen Jiang,[1,a)] Xiaoxi Duan,[1] Huan Zhang,[1] LiLing Li,[1] Weiming Yang,[1] Yonggang Liu,[1] Yulong Li,[1] Liang Sun,[1] Hao Liu,[1] and Zhebin Wang[1,a)]

AFFILIATIONS

[1]Laser Fusion Research Center, China Academy of Engineering Physics, Mianyang 621900, China
[2]Department of Plasma Physics and Fusion Engineering, University of Science and Technology of China, Hefei 230026, China

Note: This paper is part of the Special Issue on Matter in Extreme States Created by Laser.
[a)]**Authors to whom correspondence should be addressed:** jiangshn@vip.sina.com and zhebinw@vip.sina.com

ABSTRACT

In inertial confinement fusion (ICF), polycrystalline diamond—referred to as high density carbon (HDC)—has become a promising ablator candidate. However, with smaller grain size and lower initial density, the equation of state (EOS) for HDC can deviate from that for single-crystal diamond, which could be a concern for ICF designs, but current experimental EOS studies for HDC are far from sufficient to clarify how initial density affects target compressibility. Presented here are measurements of the Hugoniot for HDC with an initial density of 3.23 g/cm^3 at pressures of 17–26 Mbar. Combined with experimental data reported for nanocrystalline diamond (NCD), a stiffer compressibility of NCD due to lower initial density is confirmed. Two porous models are used for comparison and seem to offer better agreement compared with SESAME databases. Also, the effect of temperature on the Grüneisen parameter, which is usually neglected, might need to be considered for NCD under these conditions. The present data offer important support for EOS studies relevant to ICF and constrain the construction of wide-range EOS.

© 2021 Author(s). All article content, except where otherwise noted, is licensed under a Creative Commons Attribution (CC BY) license (http://creativecommons.org/licenses/by/4.0/). https://doi.org/10.1063/5.0039062

I. INTRODUCTION

Its unique properties and extensive applications make diamond an important research object in many fields, including material science, condensed matter physics, energy science and technology, and planetary science. In inertial confinement fusion (ICF),[1–3] polycrystalline diamond referred to as high density carbon (HDC)[4–6] is now a promising ablator candidate, with higher density and higher energy coupling efficiency than those of plastic (CH)[7–9] and beryllium(Be).[10–12] Using an HDC capsule, the impressive ignition milestone of fusion energy output surpassing the kinetic energy of the imploding shell has been achieved.[13–15] Because the Hugoniot of diamond crosses a complicated phase region between 6 and 11 Mbar, the first shock in ICF is designed above ~12 Mbar to eliminate the potential hydrodynamic instability seeds from this region,[16] and the pressure related to the first shock in ICF is ~1 to 5 TPa.[17–20] HDC is usually made by chemical vapor deposition (CVD) with micrometer or nanometer grain size and lower initial density than that of single-crystal diamond (SCD),[21–23] and Hugoniot variations due to these factors could be an important concern for ICF designs.

There have been numerous Hugoniot measurements of diamond in the past two decades.[24–27] Bradley *et al.*[24] measured the optical reflectivity of diamond along the principal Hugoniot, showing a continuous increase of shock reflectance from 0.6 to 1 TPa before saturation, indicating a continuous transition to metallic fluid. Nagao *et al.*[28] and Brygoo *et al.*[29] performed laser-driven Hugoniot experiments on SCD at pressures reaching 2 TPa. Hicks *et al.*[25] reported high-precision Hugoniot data for SCD at pressures of 0.6–1.9 TPa and showed good agreement between their data and *ab initio* calculations.[30,31] Knudson *et al.*[32] made diamond Hugoniot measurements at 0.55–1.4 TPa in the Sandia Z machine using the magnetic flyer-plate technique; a substantial slope change within the coexistence region provided evidence for the existence of the diamond–BC8–liquid triple point and constrained its location to between ~850 and 880 GPa. Eggert *et al.*[26] measured the diamond melting temperature along the principal Hugoniot from 0.6 to 1.1 TPa. The aforementioned studies promoted considerably the understanding of diamond properties at high pressure.

© Author(s) 2021

As mentioned before, the HDC used in ICF is not SCD but polycrystalline diamond with lower initial density and smaller grain size, but there are insufficient experimental data on HDC to provide either numerical design benchmarks or an understanding of how the initial density affects target compressibility.[33,34] Gregor *et al.*[34,35] compared the Hugoniot data for both SCD with an initial density of 3.515 g/cm^3 and nanocrystalline diamond (NCD) with an initial density of ~3.36 g/cm^3 at pressures of up to 2.6 TPa; the NCD data were stiffer than the SCD data and might be well interpreted by a porous model.

For better understanding of the initial density effects for ICF designs, Hugoniot experiments on nano-sized polycrystalline diamond with a lower initial density of ~3.23 g/cm^3 were conducted at a 10-kJ laser facility.[36] The range of experimental pressure was 1.7–2.6 TPa, which is related to the first shock strength in an HDC ablator. The Hugoniot data confirm the stiffer compression suggested by the previously reported NCD data.[34] To explain how Hugoniot data differ with initial density, porous models are used for analysis. Compared with two SESAME models, the porous models resolve the density effects better and are more sensitive to the variation of initial density in both the P–ρ and U_s–u_p planes. The deviation of the fitted Grüneisen parameter with the previous) reported value[34] suggests that temperature correction might be necessary under these conditions. The paper is organized as follows. Section II describes details of the experiments. Section III outlines impedance matching and non-steady wave correction. Data analysis and discussion are presented in Sec. IV.

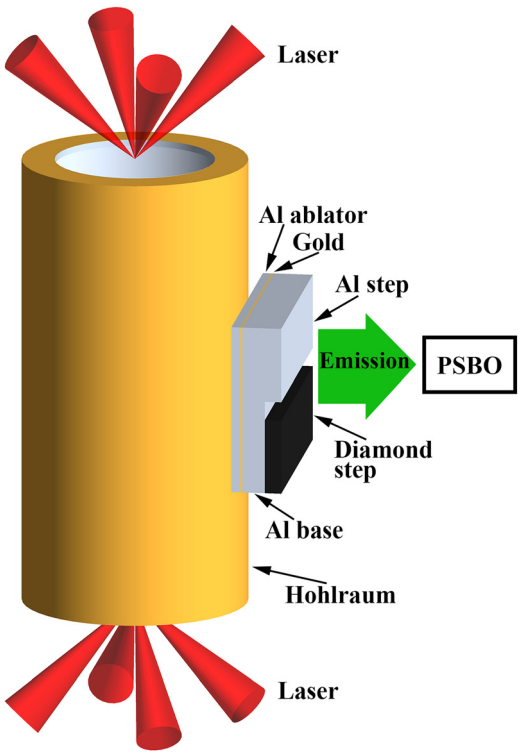

FIG. 1. Schematic of experimental configuration with impedance-matching target: PSBO, a passive shock breakout diagnostic system.

TABLE I. Thicknesses of target steps used in experiments.

Shot	Al step (μm)	HDC step (μm)
212	27.79 ± 0.35	31.95 ± 0.30
213	27.84 ± 0.27	30.43 ± 0.24
214	27.87 ± 0.23	30.78 ± 0.74

II. EXPERIMENTS

The experiments were conducted at a 10-kJ laser facility[36,37] with the experimental configuration shown schematically in Fig. 1. Higher drive uniformity was achieved via an indirect-drive scheme using a hohlraum with a diameter of 1200 μm and a length of 2400 μm. The diameter of the laser entrance hole (LEH) was 850 μm, through which eight frequency-tripled laser beams (351 nm wavelength) entered the hohlraum and were converted into an X-ray radiation field. A peak radiation temperature of 170–190 eV was achieved by a square pulse

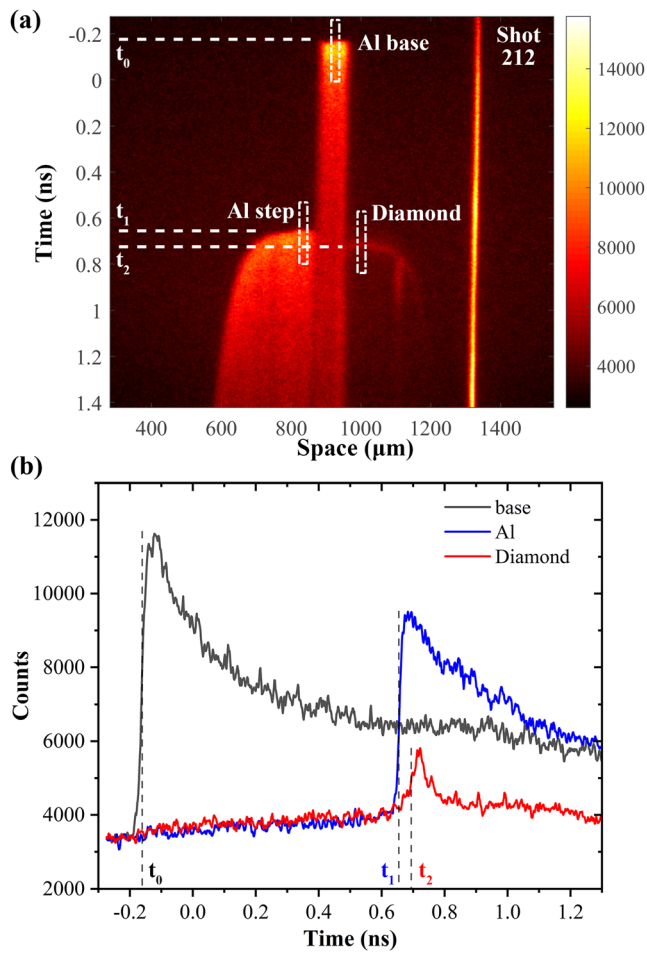

FIG. 2. (a) Streaked image of shot 212 recorded by a passive shock breakout diagnostic system (PSBO); the rightmost streak is stray light. (b) Average intensities of groups indicated in (a).

© Author(s) 2021

TABLE II. Coefficients and uncertainties of piecewise-linear form of U_s–u_p relationship $U_s = a_0 + a_1(u_p - \beta)$ for Al.[41]

Range (km/s)	$a_0 \pm \sigma_{a_0}$(km/s)	$a_1 \pm \sigma_{a_1}$	β (km/s)
$u_p \leq 6.763$	9.449 ± 0.020	1.324 ± 0.016	3.0220
$6.763 < u_p \leq 30$	17.992 ± 0.078	1.167 ± 0.026	9.8381

of 1.5 ns. The continuous-phase-plate technique[38] was used to smooth the laser beams, generating lower laser focal spot intensity and resultant preheating source strength, e.g., hot electrons and hard X rays. The target was mounted on the side of the hohlraum as shown in Fig. 1 and comprised a 15-μm aluminum (Al) ablator, a 4.5-μm gold preheat shield, and an assembly for impedance matching. The assembly comprised an Al reference substrate with thicknesses of 40 μm for the Al base and 68 μm for the Al step and a 28-μm polycrystalline diamond sample. The Al reference substrate was a monoblock made by a precision machine tool, and the nano-sized polycrystalline diamond samples were made by chemical vapor deposition (CVD).[21] The initial density of the sample was 3.23 ± 0.10 g/cm^3, and that of the Al substrate was 2.68 ± 0.01 g/cm^3. A ~100-nm-thick layer of sputtered gold foil was applied on the side of the Al substrate and the polycrystalline diamond as adhesive for thermal bonding. The gap between the Al and diamond steps was ~90 μm. For all shots, the thickness of each step was measured before the experiments and is given in Table I.

The main diagnostic instrument used in these experiments was a passive shock breakout diagnostic system (PSBO).[39,40] The temporally and spatially resolved self-emission from the rear surface of the target was recorded as a typical image shown in Fig. 2(a), where the horizontal axis is the spatial direction and the vertical axis is the temporal direction. Except for the rightmost stray light, there are three steps in the image corresponding to emission from the Al step, the Al base, and the diamond sample. For each step, the region selected for processing is divided into several groups, each comprising 16 pixels in the spatial direction. Figure 2(b) shows the average intensity variation with time from the typical groups indicated in Fig. 2(a). The shock breakout position is set as the half height of the rising edge, and the differences in shock breakout time among the groups for each step are considered in the uncertainty analysis. Combining the thickness measurement and the shock transition time gives the average shock velocities in the Al step and diamond sample.

III. IMPEDANCE MATCHING AND NON-STEADY WAVE CORRECTION

We use impedance matching to determine the particle velocity, density, and pressure of the diamond sample from the measured shock velocities in the Al and diamond. The Al principal Hugoniot with a piecewise-linear form of the U_s–u_p relationship presented in Ref. 41 is used. The coefficients and uncertainties of the U_s–u_p relationship $U_s = a_0 + a_1(u_p - \beta)$ are given in Table II.

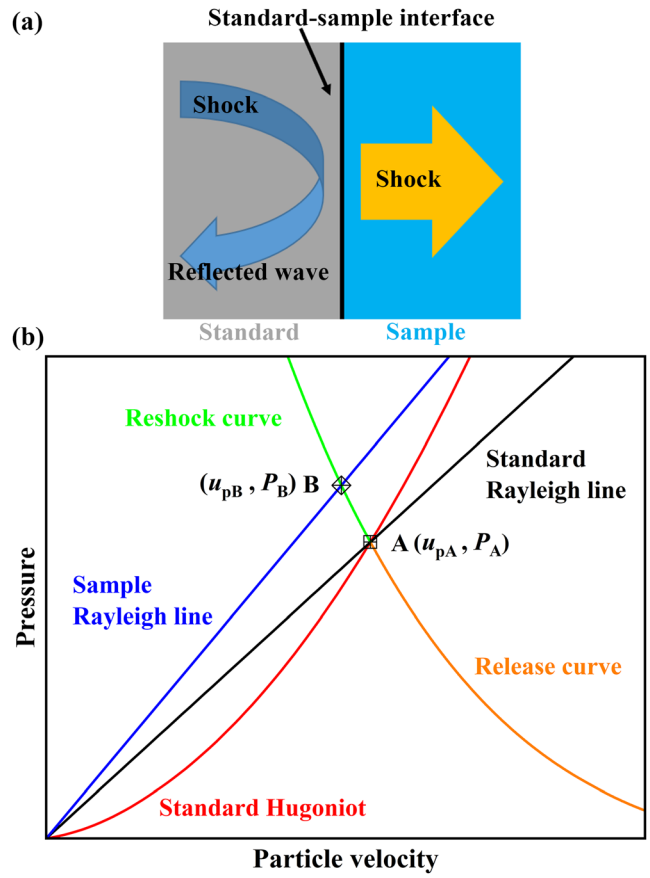

FIG. 3. (a) Shock wave propagation in standard and sample. (b) Impedance-matching analysis. Point A (u_{pA}, P_A) is the incident shock state in the standard, and point B (u_{pB}, P_B) is the Hugoniot state of the sample.

As the shock reaches the standard–sample interface as shown in Fig. 3(a), a forward-transmitted shock wave and a backward-reflected wave are launched simultaneously. The experiment determines the Hugoniot of the sample (diamond) from the initial incident shock state (u_{pA}, P_A) of the standard (Al) and the measured shock velocity of the sample. The reshock-release curve $P_R(u_p)$ of Al is approximated well by a correction on the mirror reflection $P_M(u_p)$ of the principal Hugoniot,

TABLE III. Experimental data of present study: subscripts 1 and 2 denote Al and diamond, respectively; Δt, shock transition time in Al or diamond step; U_s, measured average shock velocity; U_s^*, shock velocity with non-steady wave correction; u_p, particle velocity; P, pressure; ρ, density; U_{s1} and U_{s2}* are used in impedance matching.

Shot	Δt_1 (ps)	Δt_2 (ps)	U_{s1} (km/s)	U_{s2} (km/s)	U_{s2}^* (km/s)	u_{p2} (km/s)	P_2 (Mbar)	ρ_2 (g/cm^3)
212	818.9 ± 5.1	857.4 ± 6.7	33.94 ± 0.48	37.26 ± 0.45	37.20 ± 0.45	21.36 ± 0.63	25.67 ± 0.89	7.59 ± 0.34
213	876.2 ± 6.0	879.1 ± 7.6	31.78 ± 0.38	34.61 ± 0.41	34.51 ± 0.41	19.72 ± 0.52	21.98 ± 0.70	7.54 ± 0.31
214	977.2 ± 5.4	988.0 ± 14.4	28.53 ± 0.28	31.15 ± 0.88	31.02 ± 0.88	17.13 ± 0.44	17.16 ± 0.58	7.21 ± 0.41

© Author(s) 2021

$$P_R(u_p) = P_M(u_p) + P_C(u_p). \quad (1)$$

The pressure correction $P_C(u_p)$ is defined as

$$P_C(u_p) = P_H(u_{pA})p_n\left(\frac{u_p}{u_{pA}} - 1\right), \quad (2)$$

where P_H is the principal Hugoniot of the incident shock in Al and p_n is the correction factor expanded in Chebyshev polynomials, the coefficients of which are determined by fitting the averaged pressure corrections predicted by several theoretical equation of state (EOS) models. The scope of validity of the principal Hugoniot and the correction coefficients for Al covers the pressure range of this work. Details of the method are described by Celliers *et al.*[41] The impedance matching is shown schematically in Fig. 3(b), where the red curve is the principal Hugoniot of the standard, which is usually determined by absolute EOS measurement.[42] The Rayleigh line of the standard (black line) crosses the Hugoniot at point A, which is the incident shock state in the standard. The green curve is the reshock curve of the standard, and the Rayleigh line of the sample (blue line) crosses the reshock curve at point B, which is the Hugoniot state of the sample. The uncertainties from the measurement and fitting process are

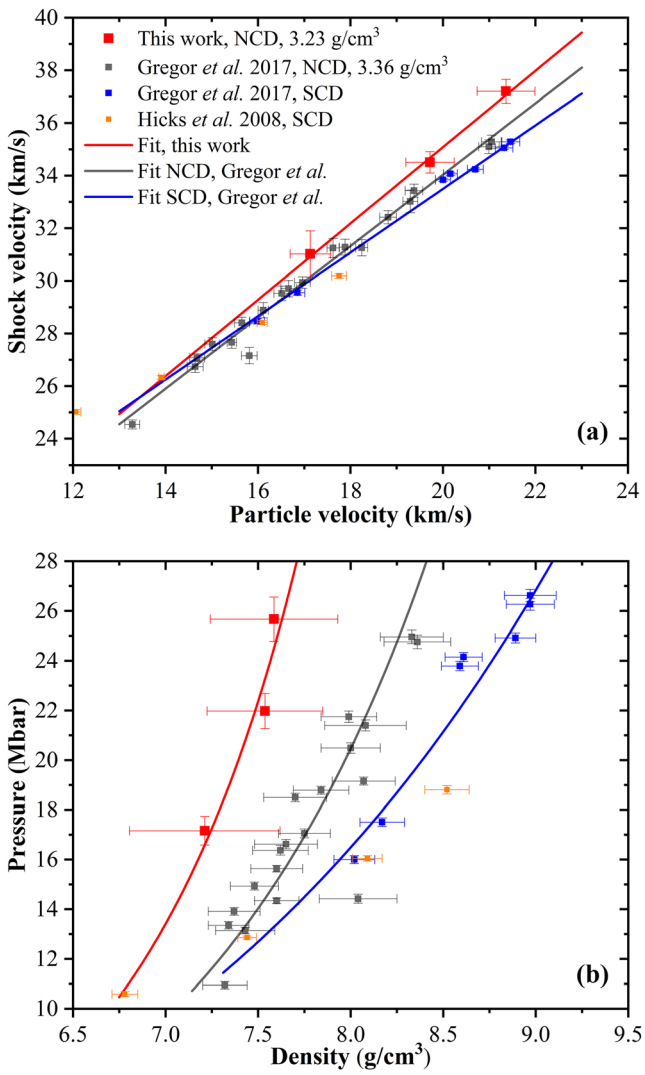

FIG. 4. Experimental data and fitted lines: (a) shock velocity vs particle velocity; (b) pressure vs density.

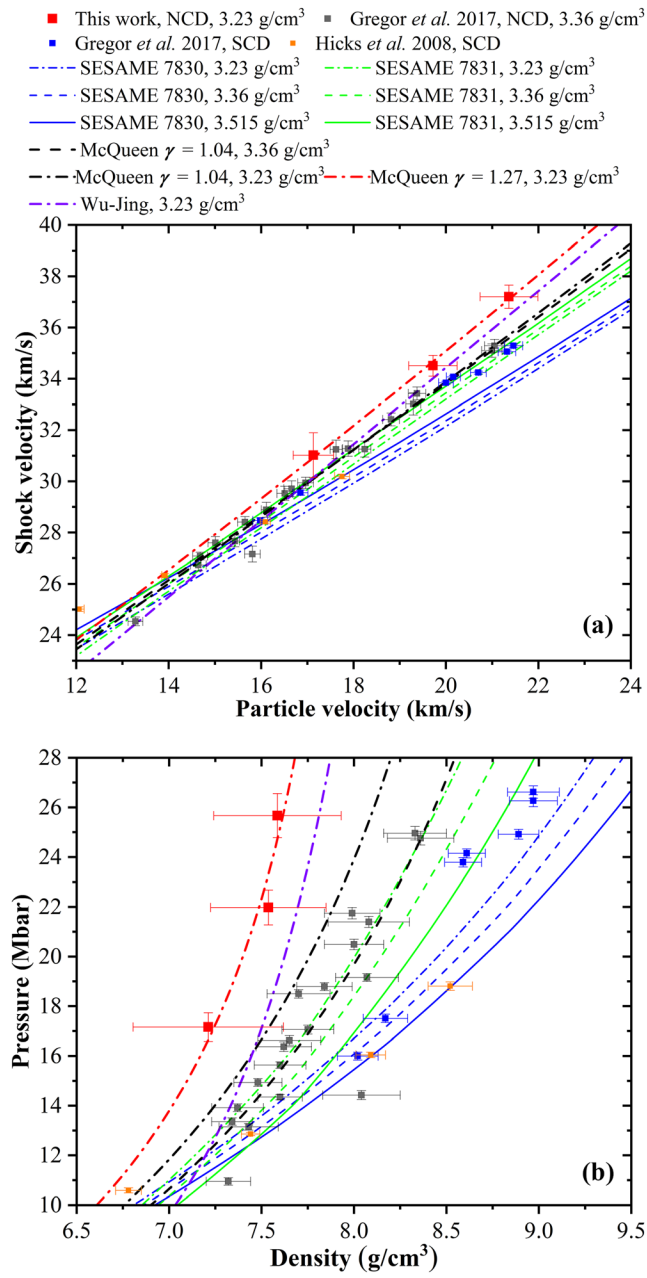

FIG. 5. Comparisons between Hugoniot data and models: (a) shock velocity vs particle velocity; (b) pressure vs density. The results of SESAME 7830 and SESAME 7831 are shown as the blue and green lines, respectively, for initial densities of 3.23, 3.36, and 3.515 g/cm^3.

© Author(s) 2021

included through the error transfer process.[41] Table III gives the impedance-matching results of this work.

Because of the complexity of laser–target interactions, the shock wave is never constant. This means that in the case of laser-driven Hugoniot experiments on opaque materials, the average shock velocities of the steps probably deviate from the instantaneous shock velocities at the standard–sample interface, which should be used in the strict impedance-matching analysis. Fratanduono *et al.*[43] proposed a theory based on a first-order perturbation analysis that could relate the perturbations at the driver surface to the shock velocity perturbations and provide the non-steady wave correction in the case of Hugoniot experiments. Duan *et al.*[44,45] developed a similar technique for shock wave correction. With this method, the average shock velocity can be used in impedance matching. This method was introduced and applied in previous Hugoniot experiments on gold foam.[45] The difference between the present study and Ref. 45 is that the former used quartz instead of CH as the witness material, and the time modulation factors F used in the present study were $F_{\text{Al-quartz}} = 1.08$ and $F_{\text{Al-Diamond}} = 0.91$. The values of the corrected shock velocity U_s^* are given in Table III.

IV. DATA ANALYSIS AND DISCUSSION

The experimental data and fitting of the present study are shown in Fig. 4, together with data reported previously for SCD and NCD with initial densities of 3.515 and 3.36 g/cm^3, respectively.[25,34,35] The Hicks data are not the original ones in Ref. 25 but the reanalyzed ones

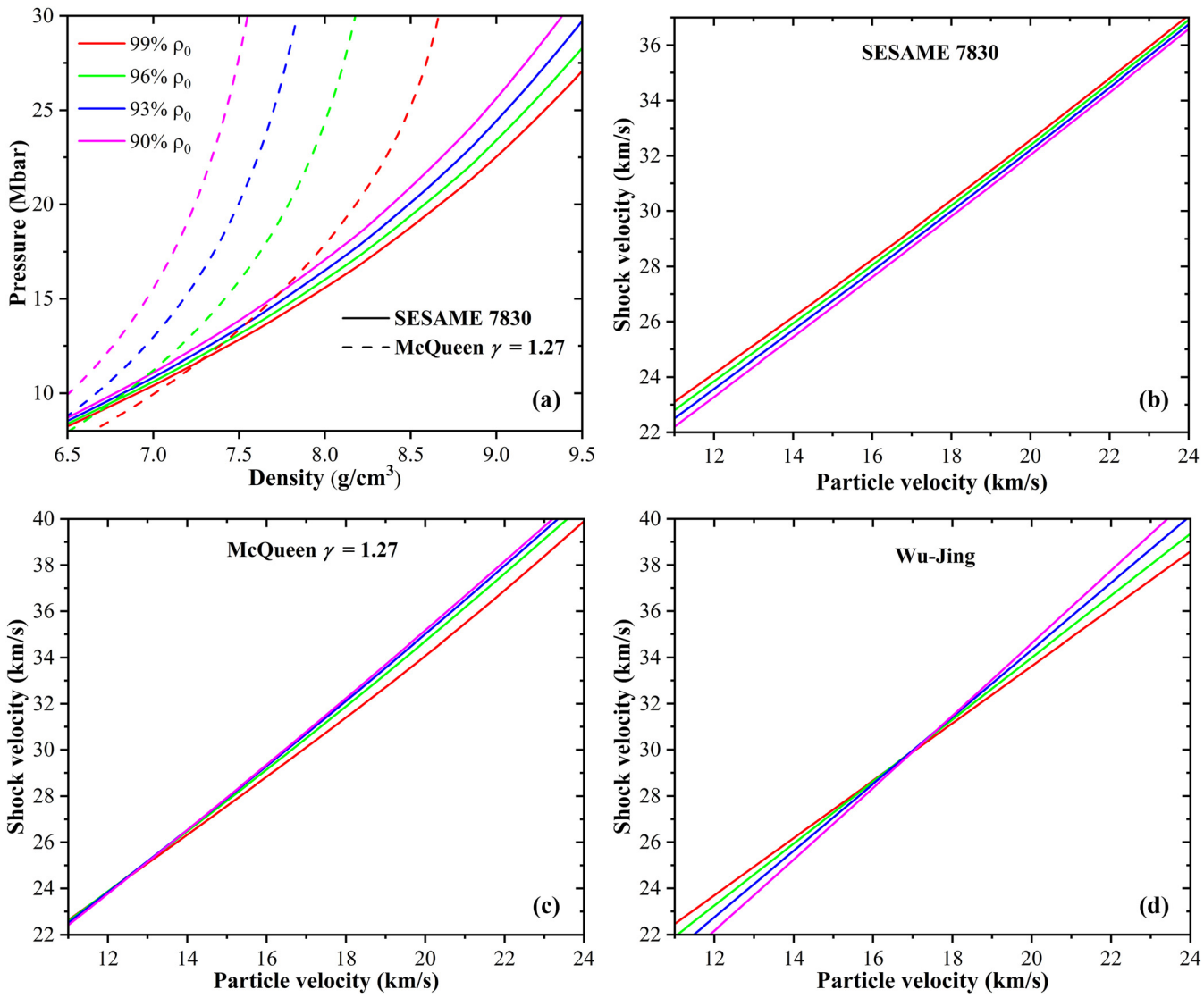

FIG. 6. Hugoniots of materials with diffeinitial density ($\rho_0 = 3.515$ g/cm^3): (a) Hugoniots from SESAME 7830 and McQueen model in P–ρ plane; (b)–(d) Hugoniots from SESAME 7830, McQueen model, and Wu–Jing model in U_s–u_p plane.

© Author(s) 2021

in Ref. 35. The linear relationships for these experimental data in the U_s–u_p plane from Ref. 34 are also shown in Fig. 5(a). The blue line is the fitted line for SCD, U_s = (30.018 ± 0.057) + (1.208 ± 0.020)(u_p − 17.12), and the black line is the fitted line for NCD (ρ_0 = 3.36 g/cm^3), U_s = (29.416 ± 0.077) + (1.356 ± 0.037)(u_p − 16.59). The shock and particle velocities of the new experimental data are fitted with the orthogonal polynomial basis[41] yielding uncorrelated errors for the coefficients and are given by

$$U_s = (34.395 \pm 0.561) + (1.450 \pm 0.348)\left(u_p - 19.524\right). \tag{3}$$

The slope of the linear relationship for diamond in the U_s–u_p plane increases moderately with decreasing initial density. The new NCD experimental data show a systematic offset from the previous results, especially at higher compression, with deviations exceeding the error-bar range. With a lower initial density of 3.23 g/cm^3, the new Hugoniot data show a tendency that is similar to that from the previous research,[34] i.e., the NCD sample has stiffer behavior compared to SCD in the P–ρ plane.

In Fig. 5, the experimental data are compared with different models including the SESAME database[46] and porous models. Two SESAME models—SESAME 7830 and SESAME 7831—are shown in Fig. 5 as the blue and green lines, respectively. SESAME 7830 is a commonly used tabular EOS model for diamond,[47,48] and SESAME 7831 is a model for liquid carbon. Both SESAME models can describe some of the SCD experimental data but apparently deviate from the NCD experimental data. Two porous models based on the Mie–Grüneisen EOS and the Wu–Jing EOS[49,50] are shown to accord better with the NCD data, indicating that the discrepancies induced by different initial densities of polycrystalline diamond might be explained by porosity effects.

The first porous model used herein is the McQueen model,[51] which is based on the Mie–Grüneisen EOS and is given by

$$P_{\mathrm{H}}^{\mathrm{Sam}}(\rho) = P_{\mathrm{H}}^{\mathrm{Ref}}(\rho)\frac{1-\frac{\gamma}{2}\left(\frac{\rho}{\rho_0^{\mathrm{Ref}}}-1\right)}{1-\frac{\gamma}{2}\left(\frac{\rho}{\rho_0^{\mathrm{Sam}}}-1\right)}, \tag{4}$$

where $P_{\mathrm{H}}^{\mathrm{Sam}}(\rho)$ is the unknown Hugoniot with initial density ρ_0^{Sam}, $P_{\mathrm{H}}^{\mathrm{Ref}}(\rho)$ is the known reference Hugoniot with initial density ρ_0^{Ref}, and γ is the Grüneisen parameter, which can be extracted from two Hugoniots of different initial densities. The reference Hugoniot of SCD is expressed by U_s = (30.018 ± 0.057) + (1.208 ± 0.020)(u_p − 17.12) from Ref. 34. γ = 1.04 ± 0.1 is found to agree well with Gregor's data at ρ_0 = 3.36 g/cm^3 in Ref. 34, and the result is shown in Fig. 5 as the black dashed line. However, the new NCD data of the present work are slightly stiffer than the McQueen model with γ = 1.04 (black dashed–dotted line), and γ = 1.27 ± 0.14 from fitting is found to agree better with the new NCD experimental data at ρ_0 = 3.23 g/cm^3, with the result shown in Fig. 5 as the red dashed–dotted line. The variation of γ with ρ_0 could be due to the fact that higher temperature is expected from the collapse of the porous structure during compression. Depending on the porosity level and initial densities, the temperature and internal energy, which could lead to different compressibility, could be different. This indicates that the Grüneisen parameter might depend on not only density but also temperature.

The other porous model is based on the Wu–Jing EOS,[49,50] which has an analogous form to the Mie–Grüneisen EOS but describes the relationship between the specific volume V and the specific enthalpy H by

$$V - V_{\mathrm{C}} = \frac{R}{P}(H - H_{\mathrm{C}}), \tag{5}$$

where the subscript C denotes the cold contribution, and R is a material parameter that is analogous to γ and depends on pressure. When studying porous Al and Cu, Nagayama[52] found that the temperature effects on R is relatively weaker than that on γ. For the pressure range studied herein, the Hugoniot of porous material deduced by Wu and Jing can be simplified as[50]

$$V_{\mathrm{H}}^{\mathrm{p}}(P) = V_{\mathrm{H}}(P) + \frac{R}{2-R}(V_{00} - V_0), \tag{6}$$

where $V_{\mathrm{H}}^{\mathrm{p}}(P)$ and $V_{\mathrm{H}}(P)$ are the Hugoniots of the porous and solid material, respectively, and V_{00} and V_0 are the initial specific volumes of the porous and solid material, respectively. Similar to the Grüneisen parameter, R can be derived from two known Hugoniots of different initial density by[52]

$$R(P) = P\frac{V_{\mathrm{H}}^{\mathrm{p}}(P) - V_{\mathrm{H}}(P)}{H_{\mathrm{H}}^{\mathrm{p}}(P) - H_{\mathrm{H}}(P)}. \tag{7}$$

Herein, $R(P)$ is calculated from the fitted Hugoniots of SCD and NCD (ρ_0 = 3.36 g/cm^3). The U_s–u_p relationship for SCD is U_s = (30.018 ± 0.057) + (1.208 ± 0.020)(u_p − 17.12), and that for NCD (ρ_0 = 3.36 g/cm^3) is U_s = (29.416 ± 0.077) + (1.356 ± 0.037)(u_p − 16.59).[34] The result of this model is shown in Fig. 5 as the violet dashed–dotted line for ρ_0 = 3.23 g/cm^3, and it lies within the error bars of the new NCD data.

For the initial-density effects of polycrystalline diamond, the porous models show larger variation in compression compared to SESAME when the initial density decreases, as seen from Fig. 6(a). In

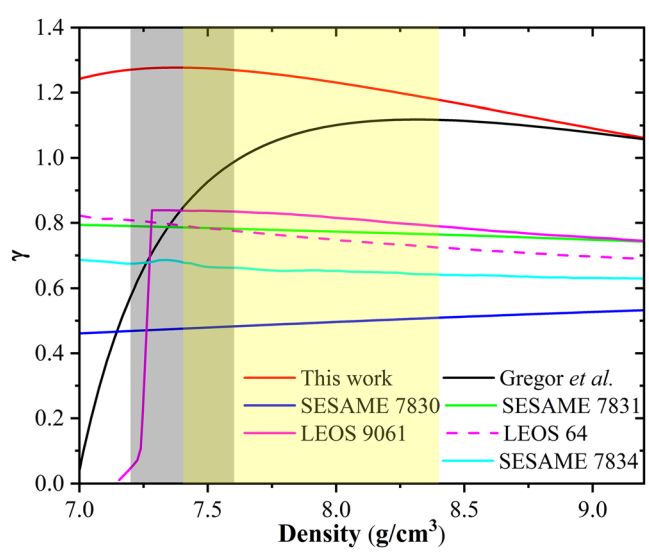

FIG. 7. Grüneisen parameter vs density. The gray and yellow regions are the valid density regions for the Grüneisen parameter of the present work (red curve) and Gregor *et al.*[34] (black curve), respectively.

© Author(s) 2021

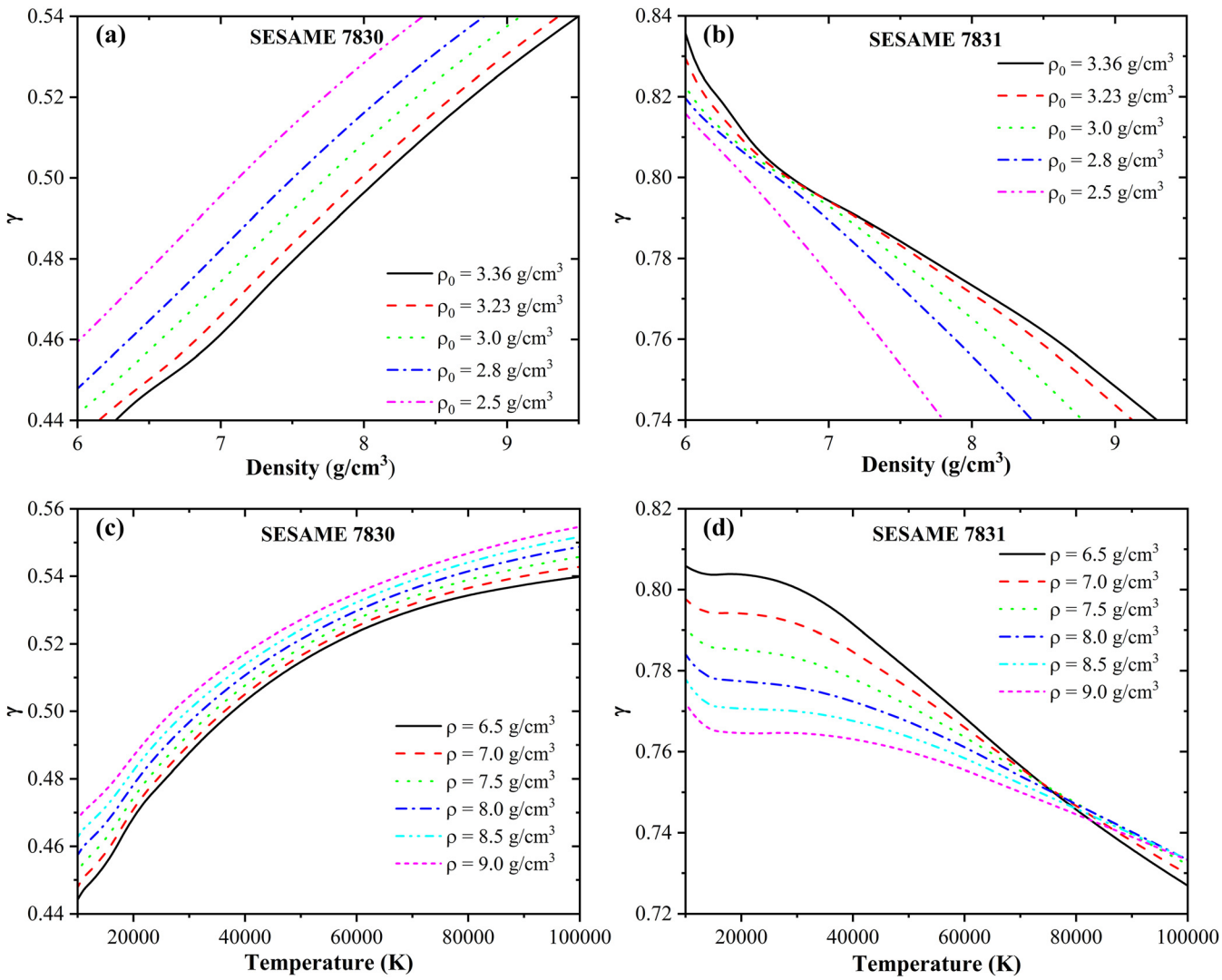

FIG. 8. (a) and (b) Grüneisen parameter calculated using Hugoniots of different initial density (full-density Hugoniot as reference) of SESAME 7830 and SESAME 7831; (c) and (d) Grüneisen parameter calculated along isochores of SESAME 7830 and SESAME 7831.

Figs. 6(b)–6(d), the slopes of the linear relationship in the U_s–u_p plane for both the McQueen and Wu–Jing models increase slightly with decreasing initial density, while the slopes of the SESAME models are almost the same. This results in intersections of U_s–u_p linearity among different initial densities for both porous models, but a set of parallel lines for the SESAME models.

Using the fitted Hugoniots for $\rho_0 = 3.23$ and 3.515 g/cm^3, $\gamma(\rho)$ is calculated and shown as the red solid curve in Fig. 7. By the same method with the fitted Hugoniots for $\rho_0 = 3.36$ and 3.515 g/cm^3, the black solid curve presented already in Ref. 34 is obtained. The values of γ calculated this way may be valid only in the region where the experimental data overlap, which is the shadow region in Fig. 7. In Ref. 34, the authors set this region to be ~7.4 to 8.4 g/cm^3 for the black curve, and the region herein for the red curve is ~7.2 to 7.6 g/cm^3. The results of LEOS 9061, LEOS 64, and SESAME 7834 are from Ref. 34. For comparison, the results of SESAME 7830 and SESAME 7831 are calculated using the Hugoniots for $\rho_0 = 3.36$ and 3.515 g/cm^3. The values of γ for the present work (red curve) and Ref. 34 (black curve) are much larger than those of the other models, and this could be related to the porosity effects, which are underestimated in the other models.

We also calculate the Grüneisen parameter by using the full-density Hugoniot and another different-initial-density Hugoniot of SESAME 7830 and SESAME 7831, and the results are shown in Figs. 8(a) and 8(b), respectively. For SESAME 7830, the lower initial density results in larger γ, and this behavior agrees with the larger γ of the present work. However, SESAME 7831 shows the opposite behavior, i.e., lower initial density results in smaller γ. Although the

© Author(s) 2021

behaviors of these two models are opposite, they both show that the value of γ calculated this way is sensitive to the variation of initial density. This might be ascribed to the difference in temperature of Hugoniots of different ρ_0, because lower initial density results in higher temperature at constant pressure along the Hugoniot. Also, in many situations, γ is assumed to depend only on density (or specific volume), but it has been noticed that γ depends also on temperature.[52,53] To explore this further, we calculate γ along some isochores of SESAME 7830 and SESAME 7831, and the results are shown in Figs. 8(c) and 8(d). In the temperature region of 10 000–100 000 K, which is pertinent to the present work, γ increases with temperature for SESAME 7830 but decreases with temperature for SESAME 7831. The results from isochores shown in Figs. 8(c) and 8(d) are self-consistent with those from Hugoniots shown in Figs. 8(a) and 8(b), respectively. The opposite temperature effects on the Grüneisen parameter for SESAME 7830 and SESAME 7831 are closely related to the modeling of these two databases, and understanding this phenomenon further will require comparing the details of their modeling. For now, Fig. 8 merely indicates that γ is temperature dependent under the present conditions, and this might explain the difference of γ between the present work and Ref. 34. Consequently, temperature effects may need to be accounted for when γ is used for the related calculation of HDC, and more studies are needed to understand fully how temperature affects γ.

V. CONCLUSIONS

In this study, indirectly laser-driven Hugoniot experiments were performed on polycrystalline diamond with an initial density of 3.23 g/cm^3. The experimental data confirm the stiffer behavior in compression of nanocrystalline diamond compared to that of single-crystal diamond. Two SESAME databases (SESAME 7830 and SESAME 7831) and porous models based on the Mie–Grüneisen and Wu–Jing equations of state were used in the analysis. Both SESAME databases underestimated the initial-density effects on the Hugoniot of polycrystalline diamond, while the porous, McQueen, and Wu–Jing models showed better agreement with the nanocrystalline-diamond experimental data. The porous models were more sensitive to the variation of initial density than the SESAME databases. Of these models, the McQueen model with a fitted $\gamma = 1.27$ best described the new Hugoniot data of the present work. We also calculated γ from Hugoniots of different initial density and along the isochores of the SESAME databases, which indicated the temperature effects on γ. This might be the reason for the difference between γ extracted herein and that done previously.[34] However, more work is still needed to understand this effect fully. The new Hugoniot data together with other experimental data for diamond could help researchers understand how initial density affects the Hugoniot of polycrystalline diamond, which could be helpful for designing and analyzing ICF research with high density carbon ablators.

ACKNOWLEDGMENTS

We thank the diagnostic instruments operation team, the laser device operation team, and the target fabrication team of the Laser Fusion Research Center for their hard work during the experiments. We also thank Longyu Kuang for his considerable help during the experiments and Qili Zhang for useful discussions. This work was supported by the National Key R&D Program of China (Grant No. 2017YFA0403201), the Science Challenge Project (Grant No. TZ2016001), and the National Natural Science Foundation of China (Grant Nos. 11805183, 12074351, and 11704351).

REFERENCES

[1] J. Lindl, "Development of the indirect-drive approach to inertial confinement fusion and the target physics basis for ignition and gain," Phys. Plasmas **2**, 3933 (1995).

[2] J. Lindl, O. Landen, J. Edwards, and E. Moses, "Review of the National Ignition Campaign 2009-2012," Phys. Plasmas **21**, 020501 (2014).

[3] J. L. Kline, S. H. Batha, L. R. Benedetti, D. Bennett, S. Bhandarkar *et al.*, "Progress of indirect drive inertial confinement fusion in the United States," Nucl. Fusion **59**, 112018 (2019).

[4] A. J. MacKinnon, N. B. Meezan, J. S. Ross, S. Le Pape, L. Berzak Hopkins *et al.*, "High-density carbon ablator experiments on the National Ignition Facility," Phys. Plasmas **21**, 056318 (2014).

[5] N. B. Meezan, L. F. Berzak Hopkins, S. Le Pape, L. Divol, A. J. MacKinnon *et al.*, "Cryogenic tritium-hydrogen-deuterium and deuterium-tritium layer implosions with high density carbon ablators in near-vacuum hohlraums," Phys. Plasmas **22**, 062703 (2015).

[6] P. Amendt, D. D. Ho, and O. S. Jones, "High-density carbon ablator ignition path with low-density gas-filled rugby hohlraum," Phys. Plasmas **22**, 040703 (2015).

[7] M. J. Edwards, P. K. Patel, J. D. Lindl, L. J. Atherton, S. H. Glenzer *et al.*, "Progress towards ignition on the National Ignition Facility," Phys. Plasmas **20**, 070501 (2013).

[8] O. A. Hurricane, D. A. Callahan, D. T. Casey, P. M. Celliers, C. Cerjan *et al.*, "Fuel gain exceeding unity in an inertially confined fusion implosion," Nature **506**, 343 (2014).

[9] O. A. Hurricane, D. A. Callahan, D. T. Casey, E. L. Dewald, T. R. Dittrich *et al.*, "The high-foot implosion campaign on the National Ignition Facility," Phys. Plasmas **21**, 056314 (2014).

[10] J. L. Kline, S. A. Yi, A. N. Simakov, R. E. Olson, D. C. Wilson *et al.*, "First beryllium capsule implosions on the National Ignition Facility," Phys. Plasmas **23**, 056310 (2016).

[11] E. N. Loomis, S. A. Yi, G. A. Kyrala, J. Kline, A. Simakov *et al.*, "Implosion shape control of high-velocity, large case-to-capsule ratio beryllium ablators at the National Ignition Facility," Phys. Plasmas **25**, 072708 (2018).

[12] A. B. Zylstra, J. E. Ralph, S. MacLaren, S. A. Yi, G. Kyrala *et al.*, "Beryllium implosions at smaller case-to-capsule ratio on NIF," High Energy Density Phys. **34**, 100747 (2020).

[13] S. Le Pape, L. F. Berzak Hopkins, L. Divol, A. Pak, E. L. Dewald *et al.*, "Fusion energy output greater than the kinetic energy of an imploding shell at the National Ignition Facility," Phys. Rev. Lett. **120**, 245003 (2018).

[14] L. B. Hopkins, S. LePape, L. Divol, A. Pak, E. Dewald *et al.*, "Toward a burning plasma state using diamond ablator inertially confined fusion (ICF) implosions on the National Ignition Facility (NIF)," Plasma Phys. Control. Fusion **61**, 014023 (2019).

[15] O. A. Hurricane, D. A. Callahan, P. T. Springer, M. J. Edwards, P. Patel *et al.*, "Beyond alpha-heating: Driving inertially confined fusion implosions toward a burning-plasma state on the National Ignition Facility," Plasma Phys. Control. Fusion **61**, 014033 (2019).

[16] S. J. Ali, P. M. Celliers, S. Haan, T. R. Boehly, N. Whiting *et al.*, "Probing the seeding of hydrodynamic instabilities from nonuniformities in ablator materials using 2D velocimetry," Phys. Plasmas **25**, 092708 (2018).

[17] D. D.-M. Ho, S. W. Haan, J. D. Salmonson, D. S. Clark, J. D. Lindl *et al.*, "Implosion configurations for robust ignition using high density carbon NIF," J. Phys.: Conf. Ser. **717**, 012023 (2016).

[18] K. L. Baker, C. A. Thomas, D. T. Casey, S. Khan, B. K. Spears *et al.*, "High-performance indirect-drive cryogenic implosions at high adiabat on the National Ignition Facility," Phys. Rev. Lett. **121**, 135001 (2018).

© Author(s) 2021

[19]D. T. Casey, C. A. Thomas, K. L. Baker, B. K. Spears, M. Hohenberger *et al.*, "The high velocity, high adiabat, "Bigfoot" campaign and tests of indirect-drive implosion scaling," Phys. Plasmas **25**, 056308 (2018).
[20]J. D. Lindl, S. W. Haan, O. L. Landen, A. R. Christopherson, and R. Betti, "Progress toward a self-consistent set of 1D ignition capsule metrics in ICF," Phys. Plasmas **25**, 122704 (2018).
[21]J. Biener, P. B. Mirkarimi, J. W. Tringe, S. L. Baker, Y. Wang *et al.*, "Diamond ablators for inertial confinement fusion," Fusion Sci. Technol. **49**, 737 (2006).
[22]J. Biener, D. D. Ho, C. Wild, E. Woerner, M. M. Biener *et al.*, "Diamond spheres for inertial confinement fusion," Nucl. Fusion **49**, 112001 (2009).
[23]C. Dawedeit, S. O. Kucheyev, S. J. Shin, T. M. Willey, M. Bagge-Hansen *et al.*, "Grain size dependent physical and chemical properties of thick CVD diamond films for high energy density physics experiments," Diamond Relat. Mater. **40**, 75 (2013).
[24]D. K. Bradley, J. H. Eggert, D. G. Hicks, P. M. Celliers, S. J. Moon *et al.*, "Shock compressing diamond to a conducting fluid," Phys. Rev. Lett. **93**, 195506 (2004).
[25]D. G. Hicks, T. R. Boehly, P. M. Celliers, D. K. Bradley, J. H. Eggert *et al.*, "High-precision measurements of the diamond Hugoniot in and above the melt region," Phys. Rev. B **78**, 843317 (2008).
[26]J. H. Eggert, D. G. Hicks, P. M. Celliers, D. K. Bradley, R. S. McWilliams *et al.*, "Melting temperature of diamond at ultrahigh pressure," Nat. Phys. **6**, 40 (2009).
[27]K. Katagiri, N. Ozaki, K. Miyanishi, N. Kamimura, Y. Umeda *et al.*, "Optical properties of shock-compressed diamond up to 550 GPa," Phys. Rev. B **101**, 184106 (2020).
[28]H. Nagao, K. G. Nakamura, K. Kondo, N. Ozaki, K. Takamatsu *et al.*, "Hugoniot measurement of diamond under laser shock compression up to 2 TPa," Phys. Plasmas **13**, 052705 (2006).
[29]S. Brygoo, E. Henry, P. Loubeyre, J. Eggert, M. Koenig *et al.*, "Laser-shock compression of diamond and evidence of a negative-slope melting curve," Nat. Mater. **6**, 274 (2007).
[30]N. A. Romero and W. D. Mattson, "Density-functional calculation of the shock Hugoniot for diamond," Phys. Rev. B **76**, 214113 (2007).
[31]A. A. Correa, L. X. Benedict, D. A. Young, E. Schwegler, and S. A. Bonev, "First-principles multiphase equation of state of carbon under extreme conditions," Phys. Rev. B **78**, 024101 (2008).
[32]M. D. Knudson, M. P. Desjarlais, and D. H. Dolan, "Shock-wave exploration of the high-pressure phases of carbon," Science **322**, 1822 (2008).
[33]K. Katagiri, N. Ozaki, Y. Umeda, T. Irifune, N. Kamimura *et al.*, "Shock response of full density nanopolycrystalline diamond," Phys. Rev. Lett. **125**, 185701 (2020).
[34]M. C. Gregor, D. E. Fratanduono, C. A. McCoy, D. N. Polsin, A. Sorce *et al.*, "Hugoniot and release measurements in diamond shocked up to 26 Mbar," Phys. Rev. B **95**, 144114 (2017).
[35]M. C. Gregor, "The shock and release behaviors of diamond at terapascal pressures," Ph.D. dissertation (University of Rochester, Rochester, 2017).
[36]S. W. Li, R. Q. Yi, X. H. Jiang, X. A. He, Y. L. Chui *et al.*, "Experimental study of radiation temperature for gold hohlraum heated with 1 ns, 0.35 μm lasers on SG-III prototype laser facility," Acta Phys. Sin. **58**, 3255 (2009).
[37]N. J. Hartley, C. Zhang, X. Duan, L. G. Huang, S. Jiang *et al.*, "Dynamically pre-compressed hydrocarbons studied by self-impedance mismatch," Matter Radiat. Extremes **5**, 028401 (2020).
[38]C. Yang, R. Zhang, Q. Xu, and P. Ma, "Continuous phase plate for laser beam smoothing," Appl. Opt. **47**, 1465 (2008).
[39]Z. Wang, X. Jiang, S. Li, H. Zhang, L. Kuang *et al.*, "Passive measurement of radiation driven shock velocity," High Power Laser Particle Beams **25**, 375 (2013).
[40]F. Wang, S. Jiang, Y. Ding, S. Liu, J. Yang *et al.*, "Recent diagnostic developments at the 100 kJ-level laser facility in China," Matter Radiat. Extremes **5**, 035201 (2020).
[41]P. M. Celliers, G. W. Collins, D. G. Hicks, and J. H. Eggert, "Systematic uncertainties in shock-wave impedance-match analysis and the high-pressure equation of state of Al," J. Appl. Phys. **98**, 113529 (2005).
[42]M. D. Knudson, R. W. Lemke, D. B. Hayes, C. A. Hall, C. Deeney *et al.*, "Near-absolute Hugoniot measurements in aluminum to 500 GPa using a magnetically accelerated flyer plate technique," J. Appl. Phys. **94**, 4420 (2003).
[43]D. E. Fratanduono, D. H. Munro, P. M. Celliers, and G. W. Collins, "Hugoniot experiments with unsteady waves," J. Appl. Phys. **116**, 033517 (2014).
[44]X. Duan, Z. Wang, C. Zhang, L. Sun, Q. Ye *et al.*, "A method for impedance-match experiments with unsteady shock loading" (unpublished).
[45]W. Liu, X. Duan, S. Jiang, Z. Wang, L. Sun *et al.*, "Laser-driven shock compression of gold foam in the terapascal pressure range," Phys. Plasmas **25**, 062707 (2018).
[46]S. P. Lyon, J. D. Johnson, "SESAME: The Los Alamos National Laboratory equation of state database," Los Alamos National Laboratory Technical Report No. LA-UR-92-3407, 1992.
[47]M. Millot, P. M. Celliers, P. A. Sterne, L. X. Benedict, A. A. Correa *et al.*, "Measuring the shock impedance mismatch between high-density carbon and deuterium at the National Ignition Facility," Phys. Rev. B **97**, 144108 (2018).
[48]M. C. Marshall, A. E. Lazicki, D. Erskine, R. A. London, D. E. Fratanduono *et al.*, "Developing quartz and molybdenum as impedance-matching standards in the 100-Mbar regime," Phys. Rev. B **99**, 174101 (2019).
[49]Q. Wu and F. Jing, "Unified thermodynamic equation-of-state for porous materials in a wide pressure range," Appl. Phys. Lett. **67**, 49 (1995).
[50]Q. Wu and F. Jing, "Thermodynamic equation of state and application to Hugoniot predictions for porous materials," J. Appl. Phys. **80**, 4343 (1996).
[51]R. G. McQueen, S. P. Marsh, J. W. Taylor, J. N. Fritz, and W. J. Carter, in *High-Velocity Impact Phenomena*, edited by R. Kinslow (Academic Press, New York, 1970).
[52]K. Nagayama, "Formulation of the Rice-Walsh equation of state based on shock Hugoniot data for porous metals," J. Appl. Phys. **119**, 195901 (2016).
[53]O. L. Anderson, "The Grüneisen ratio for the last 30 years," Geophys. J. Int. **143**, 279 (2000).

© Author(s) 2021